Comparison of mineral dust layers vertical structures modeled with CHIMERE-DUST and observed with the CALIOP lidar

Maria Raffaella Vuolo, Hélène Chepfer, Laurent Menut, Grégory Cesana

▶ **To cite this version:**

Maria Raffaella Vuolo, Hélène Chepfer, Laurent Menut, Grégory Cesana. Comparison of mineral dust layers vertical structures modeled with CHIMERE-DUST and observed with the CALIOP lidar. Journal of Geophysical Research: Atmospheres, 2009, 114 (D9), pp.D09214. 10.1029/2008JD011219 . hal-04113605

HAL Id: hal-04113605
https://hal.science/hal-04113605

Submitted on 2 Jun 2023

HAL is a multi-disciplinary open access archive for the deposit and dissemination of scientific research documents, whether they are published or not. The documents may come from teaching and research institutions in France or abroad, or from public or private research centers.

L'archive ouverte pluridisciplinaire **HAL**, est destinée au dépôt et à la diffusion de documents scientifiques de niveau recherche, publiés ou non, émanant des établissements d'enseignement et de recherche français ou étrangers, des laboratoires publics ou privés.

Copyright

Comparison of mineral dust layers vertical structures modeled with CHIMERE-DUST and observed with the CALIOP lidar

Maria Raffaella Vuolo,[1] Hélène Chepfer,[2] Laurent Menut,[3] and Grégory Cesana[3]

Received 30 September 2008; revised 25 February 2009; accepted 3 March 2009; published 13 May 2009.

[1] The final budget of dust remaining in the atmosphere or deposited on the surface depends directly on the emissions, boundary layer turbulence, stability in the troposphere, and clouds properties. The modeling of these processes remains uncertain and mineral dust long-range transport constitutes a major unknown. To improve this transport, it is crucial to improve modeling of altitudes and thicknesses of mineral dust layers. The spaceborne lidar Cloud-Aerosol Lidar with Orthogonal Polarization (CALIOP) aboard Cloud-Aerosol Lidar and Infrared Pathfinder Satellite Observations (CALIPSO) collects new information about the aerosol vertical distribution. Here we diagnose the lidar profile from the outputs of the transport model CHIMERE-DUST and we compare those with their observed counterparts. During the periods June to September 2006 and January to March 2007, the occurrences and structures of dust layers are estimated from the observed and modeled lidar signals. Accounting for the daytime and nighttime periods, the seasonal variability, and CALIPSO flight tracks, it is shown that the presence/absence of dust is correctly reproduced by the model in 70% of the 170,000 vertical profiles studied. The mineral dust horizontal distribution is quite correctly reproduced by the model, while the vertical one shows a vertical overspread which is more pronounced during winter (+100% compared to observations) than summer (+50%). The maximum value of the modeled lidar signal is underestimated with respect to the measured one by typically 30%. Multilayered dust situations are more frequent in the observations (30% of the total data set) than in the model (10%). Despite these errors, the model is able to catch the seasonal variations of the dust layers: the increases of the dust load and of the dust altitudes during summer and the northward shift of the maximum dust occurrence.

Citation: Vuolo, M. R., H. Chepfer, L. Menut, and G. Cesana (2009), Comparison of mineral dust layers vertical structures modeled with CHIMERE-DUST and observed with the CALIOP lidar, *J. Geophys. Res.*, *114*, D09214, doi:10.1029/2008JD011219.

1. Introduction

[2] Mineral dust is one of the most abundant aerosol type on the Earth surface, its global emission being estimated between 60 and 3000 Mt/a [*Duce*, 1995]. It is produced in arid and semiarid areas and then travels in the free troposphere on intercontinental scales of distance. The huge amount of mineral dust in the atmosphere leads up to a significative impact on radiative balance, both directly (through their interaction with solar and Earth radiation) and indirectly (through their influence on clouds formation and optical properties) [e.g., *Sokolik et al.*, 2001]. One of the major world dust source is the Saharan region. About 80–120 Mt/a [*d'Almeida*, 1986] of Saharan emitted dust is transported over Mediterranean sea and Europe, and 10 Mt/a [*Prospero et al.*, 1996] are transported by the trade winds over the Atlantic up to Caribbean Sea. This phenomenon brings a large amount of nutrients to phytoplankton and other marine organisms, but is also responsible for the destruction of coral reefs, as it acts as a carrier for several bacteria and fungi [*Shinn et al.*, 2000].

[3] In order to refine our knowledge of the relative amount of dust emitted, transported and deposited near or far from the sources, three-dimensional emissions and transport models are necessary. Dust transport has been widely studied at global scale [i.e., *Duce*, 1995; *Guelle et al.*, 2000; *Ginoux et al.*, 2004; *Mikami et al.*, 2006; *Zhu et al.*, 2007], and regional scales [i.e., *Ansmann et al.*, 2003; *Mona et al.*, 2006; *Grini et al.*, 2006; *Bouet et al.*, 2007; *Menut et al.*, 2007; *Kalashnikova and Kahn*, 2008]. The ability of the models to reproduce the vertical structure of the dust plumes (altitude and thickness) during their transport remains a key problem which impacts the final budget of dust in the atmosphere. Various studies [i.e., *Kishcha et al.*, 2005; *Colette et al.*, 2006; *Amiridis et al.*, 2007; *Barnaba et al.*, 2007; *Heinold et al.*, 2007] used ground-based lidar observations to evaluate the dust layers predicted by transport models. They showed that the latter are not always able to catch fine vertical structures, and that thin

[1] Laboratoire de Météorologie Dynamique, Institut Pierre-Simon Laplace, Ecole Polytechnique, Palaiseau, France.
[2] Laboratoire de Météorologie Dynamique, Institut Pierre-Simon Laplace, Université Pierre et Marie Curie, Paris, France.
[3] Laboratoire de Météorologie Dynamique, Institut Pierre-Simon Laplace, Ecole Polytechnique, CNRS, Palaiseau, France.

Copyright 2009 by the American Geophysical Union.
0148-0227/09/2008JD011219

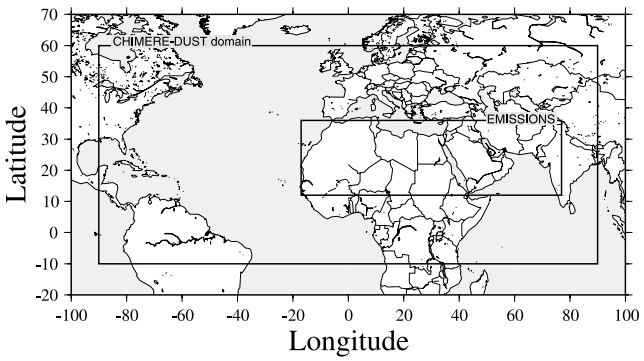

Figure 1. CHIMERE-DUST model domain. The emissions area is denoted as "EMI" and the surface in the model domain but not in the emissions area is denoted as "noEMI."

layers have an impact on the surface aerosol budget over remote areas like Europe.

[4] Lidars in space collect observations of the aerosol vertical distribution that can be used to evaluate atmospheric transport models [see, e.g., *Karyampudi et al.*, 1999]. The lidar Cloud-Aerosol Lidar with Orthogonal Polarization (CALIOP), launched in April 2006 during the Cloud-Aerosol Lidar and Infrared Pathfinder Satellite Observations (CALIPSO) mission, measures the profiles of light backscattered by aerosols with a high vertical resolution [*Winker et al.*, 2007]. It documents the aerosol vertical distribution and optical characteristics [*Z. Liu et al.*, 2008a; *D. Liu et al.*, 2008] that can be used to evaluate dust transport models. CALIPSO observations have been analyzed with complementary measurements [*Kim et al.*, 2008; *Z. Liu et al.*, 2008b] or used for the validation/evaluation of dust models [*Uno et al.*, 2008; *Hara et al.*, 2008].

[5] This study aims at evaluating the capability of the CHIMERE-DUST model to simulate the mineral dust vertical distribution and transport. The main characteristics of the model and the CALIOP observations are described in sections 2 and 3. The methodology that is used to compare consistently the model outputs with the observations is defined in section 4 together with the different characteristics of the dust layers (dust occurrence, dust load, altitudes of the upper and lower dust layers). Statistics of the observed and modeled dust characteristics are examined independently in section 5. The comparison between model and observation data sets are performed in two steps. In a first step, the two data sets are compared globally to evaluate the ability of the model to reproduce the mineral dust occurrence, and their vertical and horizontal distributions (section 6). In a second step, the dust vertical structure is evaluated in using the sub−data sets where dust layers are identified at the same time and location in model and observations (section 7). In order to better the results, the main uncertainties of the modelers are discussed in section 8. Conclusions of this study are given in section 9.

2. Description of the Model

[6] The model consists of three elements: (1) the meteorological platform with the MM5 model forced by the NCEP global meteorological fields, (2) the dust emissions model, and (3) the CHIMERE-DUST transport model. These elements are used together and in the same manner both in analysis or forecast mode. CHIMERE-DUST is a transport model dedicated to mineral dust only. It was developed on the basis of the chemistry-transport model CHIMERE [*Vautard et al.*, 2001; *Bessagnet et al.*, 2004] currently used for boundary-layer regional air pollution studies and forecast. The complete model characteristics are described by *Menut et al.* [2007].

2.1. Meteorological Forcing

[7] Since CHIMERE-DUST is an offline model, meteorological fields are required: for this study, the NCEP/GFS meteorological fields are used to force the regional mesoscale model MM5 [*Dudhia*, 1993]. The outputs of MM5 have an horizontal resolution of $1^\circ \times 1^\circ$, with 32 vertical levels, from surface to 200 hPa. The horizontal domain (Figure 1) covers the whole North Atlantic Ocean, including a large part of northern Africa and of western Europe. The results of MM5 simulations (wind components, temperature, specific humidity, pressure fields, 2-m temperature and sensible and latent surface heat fluxes) are used to diagnose additional turbulent parameters such as the boundary layer height $\overline{h}$, the friction velocity u_* using a bulk Richardson profile approach [*Menut*, 2003], and the water liquid content (for the wet deposition). These parameters are used to estimate the vertically averaged meteorological profiles (switching from 32 to 15 vertical levels) for the CHIMERE-DUST configuration.

2.2. Transport Model CHIMERE-DUST

[8] CHIMERE-DUST is driven by MM5 meteorological fields at an hourly time step and over the same horizontal domain ($1^\circ \times 1^\circ$ resolution). As the domain is sufficiently large to include all the major dust sources, the boundary conditions are not taken into account for the dust. The dust concentration is initialized to zero at the first time step, but we consider a long spin-up time (15 days before the first date of interest) in order to study realistic dust concentrations. The horizontal transport is computed using the Van Leer scheme [*Van Leer*, 1979]. The dust simulations are performed with a $7'30''$ time step, and the dust concentrations are extracted every hour for analysis.

2.3. Dust Emissions Calculation

[9] The emissions scheme used in the model is first based on the *Marticorena and Bergametti*'s [1995] dust production model. This model is used to compute horizontal fluxes from wind velocities and surface features for the emissions area (Figure 1). Then, the dust vertical fluxes is derived from the horizontal fluxes by using the *Alfaro and Gomes* [2001] parameterization, numerically optimized after *Menut et al.* [2005]. The vertical fluxes are computed for three dust size modes and redistributed into the model size bins using the following mass partition scheme:

$$m_i = \sum_n \frac{m_n}{2} \left| \mathrm{erf}\left(\frac{\ln d_{i,l}/Dp_n}{\sqrt{2}.\ln \sigma_n}\right) - \mathrm{erf}\left(\frac{\ln d_{i,u}/Dp_n}{\sqrt{2}.\ln \sigma_n}\right) \right|, \quad (1)$$

where m_i and m_n are the emitted masses in the model bins and in the three emitted modes, respectively. Dp_n and σ_n are the emitted mass diameters and associated standard deviations (as described by *Menut et al.* [2005]); $d_{i,l}$ and

21562202d, 2009, D9, Downloaded from https://agupubs.onlinelibrary.wiley.com/doi/10.1029/2008JD011219 by Cochrane France, Wiley Online Library on [02/06/2023]. See the Terms and Conditions (https://onlinelibrary.wiley.com/terms-and-conditions) on Wiley Online Library for rules of use; OA articles are governed by the applicable Creative Commons License

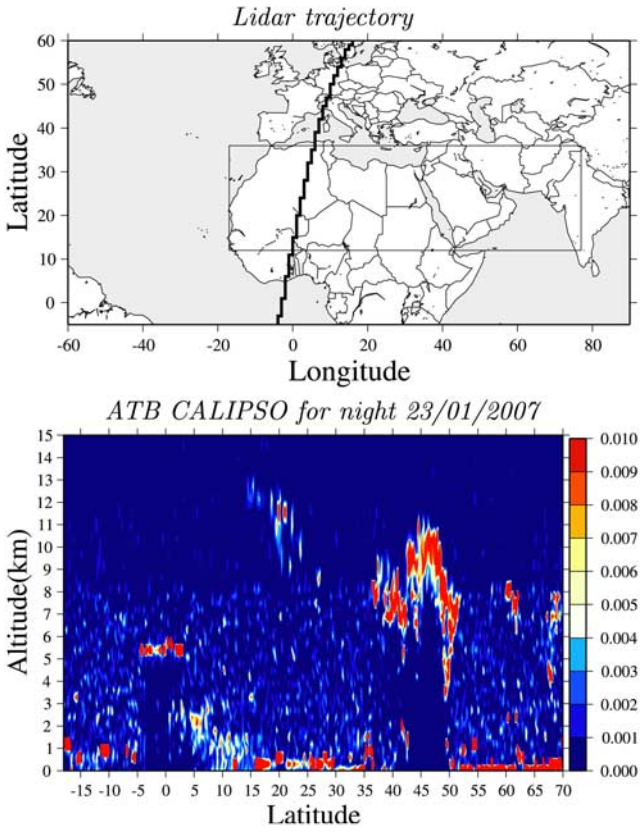

Figure 2. (top) CALIOP lidar trajectory aboard CALIPSO for 23 January 2007 and (bottom) the corresponding measured ATB (m^{-1} sr^{-1}).

$d_{i,u}$ are the diameter of the lower and upper limits of each dust size bin, respectively.

[10] The wet deposition scheme is described by *Loosmore and Cederwall* [2004]. The dry deposition velocity is parameterized following *Venkatram and Pleim* [1999].

3. Description of CALIOP Observations

[11] The CALIOP lidar is composed of a laser, which emits two beams of linearly polarized light at 532 nm and 1064 nm, and a telescope that collects the laser light backscattered by molecules and particles at each level of altitude [*Winker et al.*, 2007]. The intensity of the backscattered attenuated signal (ATB) depends on the aerosol vertical distribution while the depolarization ratio is related to their shape. At λ = 532 nm, CALIOP horizontal resolution is 333 m below 8 km altitude and 1 km above.

[12] CALIPSO platform follows a Sun-synchronized orbit with an equatorial crossing time of about 0130 and 1330 LST. The current study uses the CALIOP Version 2.01 Level 1 data set at 532 nm collected within the CHIMERE-DUST domain in summer 2006 (June to September) and winter 2007 (January-February-March) during daytime and nighttime. Figure 2 shows an example of the satellite trajectory and the corresponding CALIOP observations for 23 January 2007.

[13] The ATB_{mol} profile represents the signal that would be measured by the lidar in the absence of aerosols and clouds. It is computed with local values of pressure and temperature profiles from Global Modelling and Assimilation Office (GMAO) [*Bey et al.*, 2001]. The measured ATB and the computed ATB_{mol} profiles are averaged independently over the CHIMERE-DUST horizontal and vertical grid; it increases significantly the signal to noise ratio (about 240 to 300 level 1 Caliop profiles are averaged in each model grid box). Then, the averaged measured ATB profile is scaled to the averaged molecular one (ATB_{mol}) in the stratosphere (30–34 km) where the atmosphere is generally free of aerosols. The lidar backscattering ratio profile LBR = ATB/ATB_{mol} is computed from the two averaged profiles in each CHIMERE-DUST grid box along the satellite orbit track (Figure 3a). This LBR acronym is also commonly called Scattering Ratio SR in the literature; it highlights the contribution of the particles to the lidar signal.

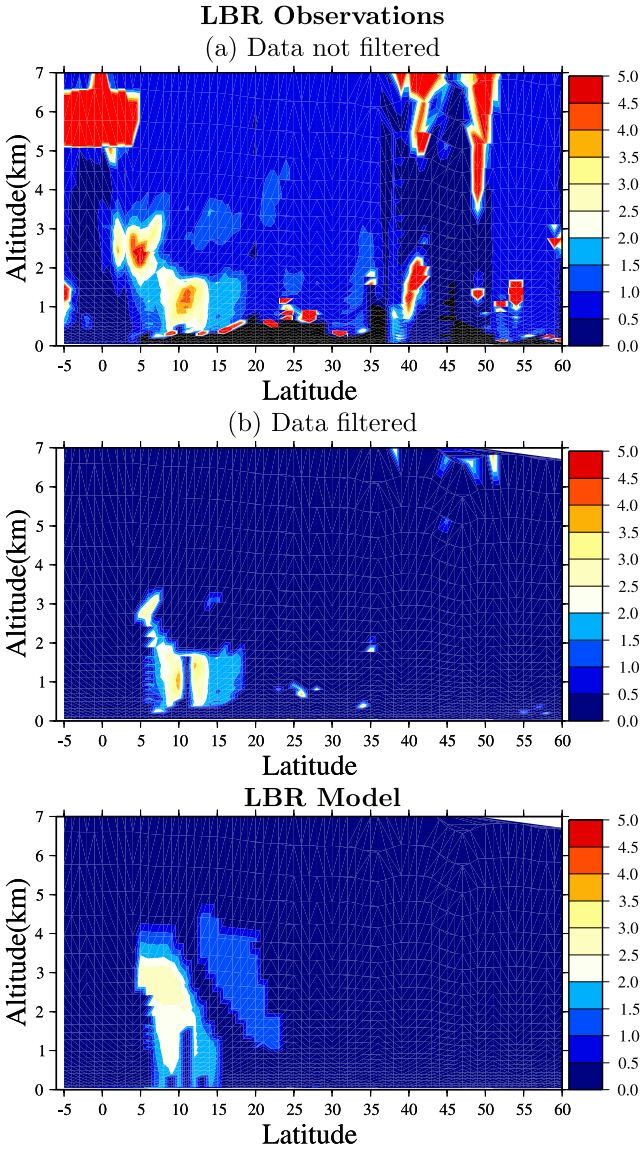

Figure 3. Analysis of the 23 January 2007 (0100 UTC) lidar data. (a) Observed LBR backscattering ratio (adimensional) averaged on CHIMERE grid but not filtered. (b) (top) Same as Figure 3a but filtered and (bottom) modeled LBR backscattering ratio (adimensional).

21562202d, 2009, D9, Downloaded from https://agupubs.onlinelibrary.wiley.com/doi/10.1029/2008JD011219 by Cochrane France, Wiley Online Library on [02/06/2023]. See the Terms and Conditions (https://onlinelibrary.wiley.com/terms-and-conditions) on Wiley Online Library for rules of use; OA articles are governed by the applicable Creative Commons License

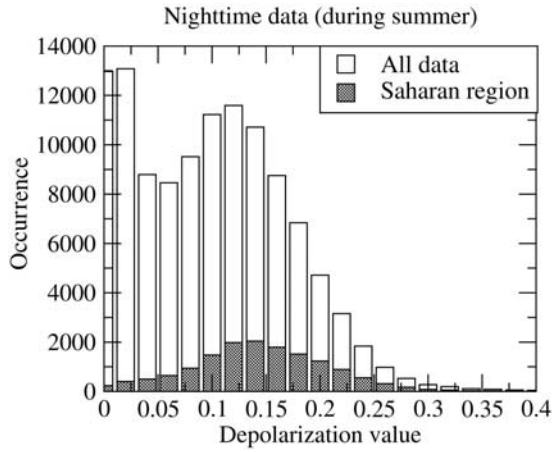

Figure 4. Distribution of measured depolarization values for the period June to September 2006. Only nighttime data are used. Occurrences are displayed for the whole domain and a subregion called "Saharan" and defined as $-15 <$ longitude < 30; $13 <$ latitude < 32. Both the dust detection and the depolarization ratio are computed over the model grid box.

[14] The ATB has two components: the first one is linearly polarized in the same direction as the incident laser light, and the other one is polarized perpendicularly. Each component is first averaged independently over the model grid box. The ratio between the intensities of these two components gives the lidar depolarization ratio, which is commonly used to distinguish dust from other aerosol types [*Z. Liu et al.*, 2008b]. Figure 4 shows a statistical comparison between the aerosol depolarization measured within the whole CHIMERE-DUST domain and a sub–data set corresponding to the region centered on emission regions. It shows that at this resolution and in this region, the Saharan dust mostly correspond to depolarization ratio higher than 10%.

4. Methodology

4.1. Simulation of Lidar Signal From Model Outputs

[15] To make a fully consistent statistical comparison between model and observations, we adapted a method used to evaluate aerosols in CHIMERE [*Hodzic et al.*, 2004] and clouds in MM5 [*Chiriaco et al.*, 2006; *Chepfer et al.*, 2007]. It consists in diagnosing the LBR as an output of the model in using pressure, temperature and dust mass concentrations fields from CHIMERE-DUST (see Appendix A).

[16] The molecular component of the LBR at $\lambda = 532$ nm is simulated using the MM5 local values of pressure and temperature. The particle component of LBR requires the computation of their number concentration and their optical properties (scattering and extinction cross sections). The latter are computed with the Mie theory [*Mie*, 1908] for 400 values of aerosols diameters ranging between 0.01 to 40 μm. The spherical assumption (Mie theory) can produce errors when applied to mineral dust aerosol owing to their nonsphericity. The mineral dust mass concentration is simulated by the model in 12 different size bins ranging between 0.1 and 50 μm [*Forêt et al.*, 2006]. The mineral dust number concentration in each bin is then computed assuming the particles are spherical and their density is 2.65 g cm^{-3}. A linear interpolation within the 12 bins allows derivation of the dust number concentration for each of the 400 particle sizes for which the scattering and extinction cross sections have been tabulated previously.

[17] The values of molecules and particles scattering and extinction coefficients are used to compute local values of LBR within the model cells located along the satellite orbit track at the time of the CALIPSO overpass (see Appendix A for the detailed computation of LBR).

4.2. Mineral Dust Characteristics Diagnostics

[18] Various mineral dust characteristics are diagnosed consistently in observations and simulations.

[19] One observed or simulated LBR profile contains 30 successive layers. The CALIOP observations data are projected on these vertical levels in order to have the same data set than with the model. First, each layer of each profile is labeled following *Chepfer et al.* [2008]. Second, the whole set of labels for one profile is used to infer the "dust occurrence" (section 4.2.2), the "profile classification" (section 4.2.3), and the "vertical structure" (section 4.2.4).

4.2.1. Layer Classification

[20] The first step is to label independently each layer of each profile for both model and observations.

[21] For the observations, each layer is classified as "clear" or "cloudy" or "dust." These three classes will be used for statistics on the observations only (for the model, only "clear" and "dust" are defined and used).

[22] For the observations profiles, the starting point is to exclude not useful layers. This class is called "cloudy" and contains all layers with clouds and/or dust not relevant for the comparisons with the model results. Three criteria are applied: (1) a minimum in temperature to avoid cirrus clouds ($temp_{obs}$ must be greater than -30°C), (2) a minimum in depolarization ratio to avoid aerosols other than those modeled by CHIMERE-DUST ($depol_{obs}$ must be greater than 0.1) and (3) a maximum of LBR to avoid water clouds (LBR_{obs} must be lower than 4).

[23] For all other layers, a subclassification is done: "clear" or "dust." The "clear" layers are defined for $LBR_{obs} \leq 1.2$ and the "dust" for $1.2 < LBR_{obs} \leq 4$. The LBR threshold values used here can lead to classify some optically thick dust plume as cloudy, but ensure the rejection of all water clouds (Figure 3b). The threshold on $depol_{obs}$ can lead to underestimate the total dust load (up to 20% based on section 4) but ensures the rejection of nondust layers (not predicted by the model). On the other hand, the term "clear" is not really a clear atmosphere but define dust-free layers.

[24] Finally, the same criteria are used on modeled dust concentrations outputs and only for model cells corresponding to CALIOP measurements.

4.2.2. Dust Occurrence

[25] For each observed and simulated grid box, we define the dust occurrence $N_{a,obs/mod} = 1$ if the layer is "dust" and 0 if not. The seasonal dust occurrences are thus defined as the sum of all $N_{a,obs/mod}$ within a latitude band and during a season (Figure 5).

21562202d, 2009, D9, Downloaded from https://agupubs.onlinelibrary.wiley.com/doi/10.1029/2008JD011219 by Cochrane France, Wiley Online Library on [02/06/2023]. See the Terms and Conditions (https://onlinelibrary.wiley.com/terms-and-conditions) on Wiley Online Library for rules of use; OA articles are governed by the applicable Creative Commons License

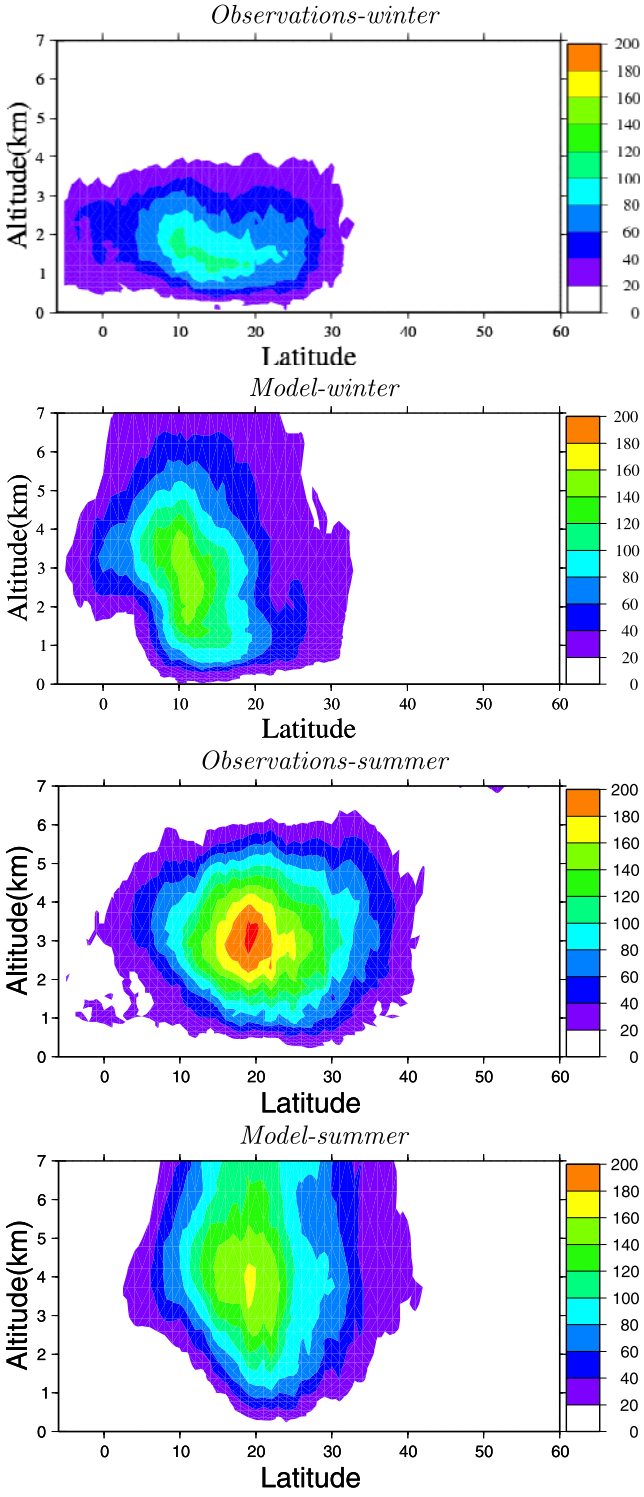

Figure 5. Zonally summed dust occurrence over the whole domain during the period January–March 2007 and June–September 2006 for all nighttime profiles observed and simulated.

4.2.3. Profile Classification

[26] From all layer classes, some profiles classes are defined. For the comparisons between model and observations, only three classes are necessary: clear, dust and cloud. The "cloud" class will only be used for observations statistics. The "clear" class is defined when a profile has only "clear" layers. The "dust" class is defined when a profile has only one or several "dust" layers. An intermediate class "dust+cloud" is defined when a "dust" layer is observed above a "cloud" layer. This profile can be partly used for analysis: since the CALIOP instrument is a nadir lidar, a dust layer above a cloud layer may be accurately identified. This profile is used for the "dust occurrence" statistics. But, if a "cloud" layer is identified with no "dust" above, the complete profile is considered as "cloud" and not used for statistics. In this case, and even if dust are present under the cloud, a doubt exists owing to the signal perturbation due to the cloud layer. A refinement is done using the "cloud" layer altitude. If the layer is up to 8 km, the profile label is "high cloud." For all other cases, the label is "low cloud."

4.2.4. Vertical Structure Diagnostics

[27] We also evaluate the integrated value of LBR over the "dust" cells (LBR_{int}, in kilometers), the local maximum value of LBR (LBR_{max}) and its corresponding altitude (z_m). The dust layer thickness is estimated as the sum of the layers with "dust" (no necessary successive) and is denoted *th*. In the same way, the heights of the lower and upper dust layers are estimated and noted z_l and z_t, respectively. These quantities are computed in considering only the "dust" and "clear" layers in each profiles. LBR_{int} and LBR_{max} depend mostly on the dust concentration and optical properties (these latter being directly related to their size), whereas z_m, *th*, z_l and z_t are directly influenced by the vertical transport (advection and mixing).

5. Analysis of Observed and Modeled Dust Layers

[28] The diagnostics presented are applied to all the observed and simulated profiles along the CALIPSO orbits crossing the CHIMERE-DUST domain during the "summer" (June to September 2006) and the "winter" periods (January to March 2007). In order to help the statistical analysis, the modeled and observed data sets are split into "EMII" area (corresponding to the "emissions" region in Figure 1) and the "noEMI" area corresponding to all others domain grid cells.

5.1. Statistics on the Observations

[29] Table 1 gives the total number of profiles and their classification (defined in section 4.2.3). A significant amount of the profiles are contaminated by the presence of clouds. The profiles classified "dust" and "dust + clouds" represent more than 50% of the total number of profiles over the emissions regions ("EMI") whatever the season for both daytime and nighttime. Far from the sources ("noEMI" regions), they represent less than 30% of the profiles. The high-altitude clouds contaminate 5 to 18% of the profiles. These clouds are more numerous in summer (than winter) because they are produced by deep convection along the ITCZ. Moreover, their seasonal variation is more pronounced over land (EMI regions) than over ocean (noEMI) Over ocean, neither the fraction of high cloud profiles neither the total fraction of cloudy profiles shows a seasonal

21562202d, 2009, D9, Downloaded from https://agupubs.onlinelibrary.wiley.com/doi/10.1029/2008JD011219 by Cochrane France, Wiley Online Library on [02/06/2023]. See the Terms and Conditions (https://onlinelibrary.wiley.com/terms-and-conditions) on Wiley Online Library for rules of use; OA articles are governed by the applicable Creative Commons License

Table 1. Statistics of Observed Clouds and Dust Layers[a]

	Total	Cloud		Dust + Cloud	Dust	Clear
		High	Low			
			Winter			
EMI night	7877	5%	21%	35%	20%	19%
EMI day	8116	5%	14%	38%	23%	20%
noEMI night	40964	14%	53%	7%	11%	14%
noEMI day	40165	13%	39%	11%	22%	15%
			Summer			
EMI night	8384	18%	21%	29%	22%	10%
EMI day	8890	15%	18%	32%	28%	8%
noEMI night	41426	13%	47%	10%	15%	14%
noEMI day	44641	13%	35%	13%	28%	10%

[a]Dust refers to dust without clouds, and low cloud refers to profiles with low clouds only (no dust). The sum of the five categories is 100%.

variation. The low-level oceanic clouds are numerous all along the year, and they contribute to contaminate a significant part of the profiles over noEMI regions.

[30] The profiles not contaminated by clouds are classified as "dust" and "clear": they represent less than half of the full data set over EMI and even less (<30%) over noEMI regions. When considering only these situations, the relative part of dust containing profiles [dust/(dust + clear)] is larger in summer than winter, consistent with *Z. Liu et al.* [2008a]. The percentage of profiles containing only "dust" does not show significant day/night differences; moreover its seasonal variation over EMI regions is mostly governed by the cloud seasonal cycle.

5.2. Statistics on Modeled Dust Layers

[31] Dust occurs in 53% to 63% of profiles above EMI and 3.5 to 6 times less (12% to 16%) above noEMI (Table 2). The day/night difference is negligible. More dust is produced by the model in summer than winter above emission regions (differences of 10–15%). Far from the sources, the tendency is not the same, and more dust is detected during winter than during summer (differences of less than 4%). This may be due to different dynamical processes in the free troposphere, reducing the main sinks such as the precipitation and thus the dust scavenging.

6. Comparison Between Simulated and Observed Dust "Without Collocation Constraint"

6.1. Global Dust Occurrence

[32] The zonal dust occurrence (defined in section 4.2.2) observed and simulated over the whole CHIMERE-DUST domain in both seasons (Figure 5) shows that the dust sources are quite well localized in the model and that the increase of global dust occurrence in summer is also represented by the model.

[33] The dust occurrence is larger in summer than in winter because of the higher activity of dust sources in this season [*Prospero et al.*, 2002]. This variation is reproduced by the model, even if global dust occurrence seems slightly overestimated in winter and underestimated in summer. Nevertheless, dust is not sufficiently transported to the northern latitudes in winter, while in summer the occurrence is underestimated in the sources latitudes. Dust is vertically transported significantly too high in altitude whatever the season.

[34] The region of maximum dust occurrence is in the latitude belt 15°N–25°N and it is shifted southward in summer (8°N–18°N). This is consistent with the observations of *D. Liu et al.* [2008] and this shift follows the ITCZ position [*Prospero et al.*, 1981] as well as the location of the most active dust sources [*Prospero et al.*, 2002].

[35] The observed meridional dust occurrence (Figure 6) also shows a significative increase in summer, especially at longitudes ~40°E–60°E. The model roughly reproduces this behavior, but with an underestimate of the summer dust occurrence around ~10°W–20°E. Compared to Figure 5, results confirm a model underestimation for the region corresponding to the western Africa sources (with a mean latitude of 20°N and a mean longitude of 0° to 10°W).

6.2. Global Dust Vertical Distribution

[36] The characteristics of the dust vertical distribution (Table 3) are computed in considering only the profiles which contain dust (see Table 1 (dust + clear) for the observations).

[37] The dust load (proportional to LBR_{int}) shows an important variability: it is larger during summer than winter and larger over EMI than noEMI regions. Contrarily to LBR_{int}, the value of LBR_{max} is relatively constant in space and time, which means that the maximum amount of dust within a layer at a given altitude does not depend on the season and the location. Thus, the variation of the dust load in the column (LBR_{int}) is associated with a variation of the vertical extent of the dust plume: *th* values increase (and decrease) with LBR_{int} values. The mean layer thickness reaches a maximum of 2.3 km during summer in EMI area, compared to about 1 km for the other cases. The mean layer thickness increase is mainly due to an increased top level of these layers, when the lowest ones stay around 1 to 2 km in altitude, consistent with the findings of *Carlson and Prospero* [1972]. This is likely due to the enhanced boundary layer convection in summer that inject higher quantity of dust in the free troposphere (increasing LBR_{int} above the emission regions) at higher altitudes (increasing z_t) and can be transported over long distances (increasing LBR_{int} above noEMI).

[38] The summer reduction of z_t (Table 3) when passing from EMI to noEMI areas is due to the subsidence of the Saharan dust layer in its westward pathway [*Carlson and Prospero*, 1972]. In winter, z_t increases when passing from EMI to noEMI areas. A possible explanation is the increased efficiency of northward dust transport during winter and spring with respect to the westward one [*Dayan et al.*, 2008]: the Mediterranean dust layers are known to penetrate

Table 2. Modeled Profiles Containing Dust[a]

	Model Statistics	
	Winter	Summer
EMI night	53%	63%
EMI day	56%	70%
noEMI night	15%	12%
no EMI day	16%	12%

[a]The total number of profiles is the same as in Table 1.

21562202d, 2009, D9, Downloaded from https://agupubs.onlinelibrary.wiley.com/doi/10.1029/2008JD011219 by Cochrane France, Wiley Online Library on [02/06/2023]. See the Terms and Conditions (https://onlinelibrary.wiley.com/terms-and-conditions) on Wiley Online Library for rules of use; OA articles are governed by the applicable Creative Commons License

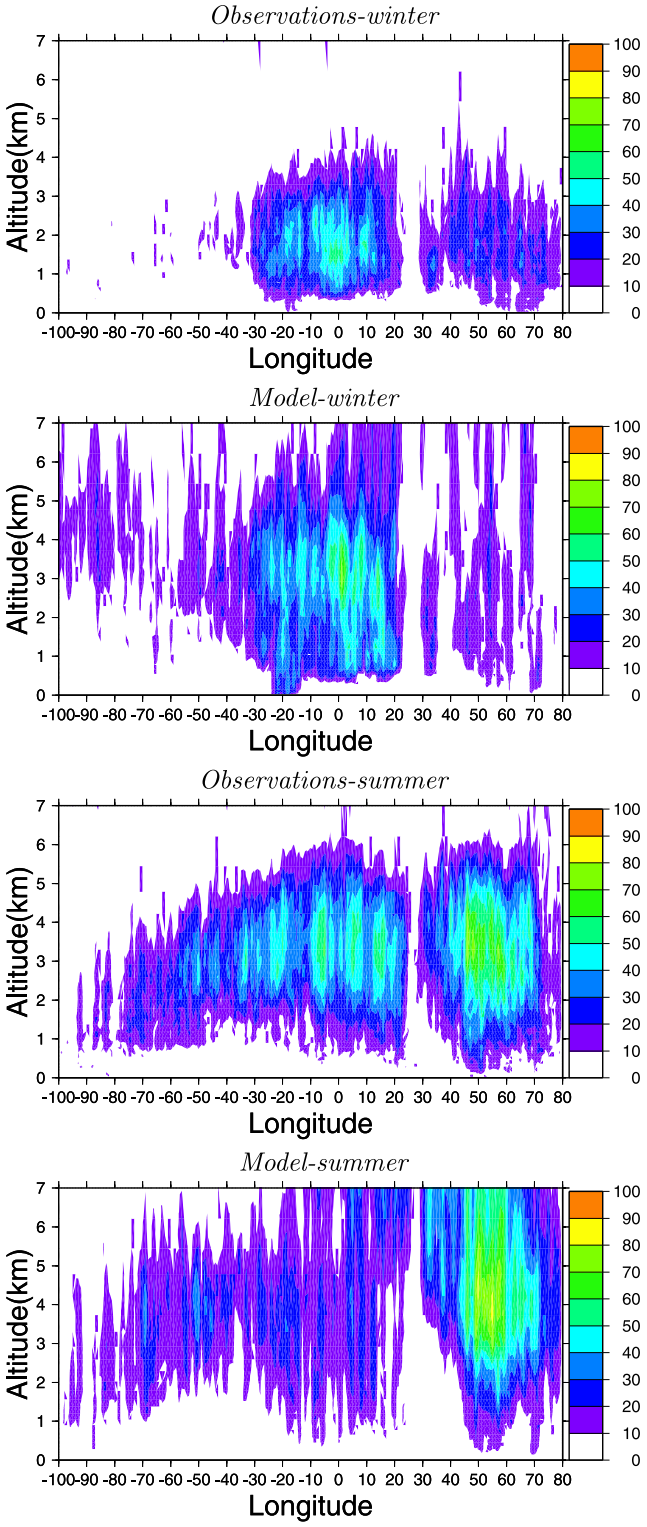

Figure 6. As in Figure 5 but with meridional sum of the dust occurrence.

higher into the troposphere than the ones transported across the Atlantic [*Hamonou et al.*, 1999; *Alpert et al.*, 2004]. This tendency of summer (winter) reduction (increase) of z_t from EMI to noEMI regions is reproduced by the model, although there are significant discrepancies in the absolute values.

[39] On average (Table 3), the dust load (LBR_{int}) is larger in the model than in the observation and simultaneously LBR_{max} is underestimated in the model; it suggests that the dust vertical distribution is too spread in the model. This is confirmed by *th* which is overestimated by 50% to 100% whatever the season and the region.

[40] Figure 7 shows that multilayer dust situations are frequently observed (typically 2 or 3 dust layers separated by clear layers), consistent with the findings of *Hamonou et al.* [1999]. The model produces more single layers than observed and is able to reproduce half of the complex multilayer structures.

6.3. Global Dust Horizontal Pattern

[41] The spatial distribution of the dust plume during summer is illustrated in Figure 8. Both the observations and model show the Saharan dust plume spatial extent over the Atlantic Ocean. The top altitude, z_t, westward decrease illustrates the subsidence of the Saharan air layer [*Carlson and Prospero*, 1972] far from the sources. The z_t is larger than 5 km above the main emission regions, and shows a maximum of 3 km above the Atlantic Ocean. The lowest variability of z_l (≈1 km both for model and observations) induces a regular decrease of the layer thicknesses, *th*.

7. Comparison Between Model and Observations When Mineral Dust Is Collocated

7.1. Dust Occurrence for the Collocated Data Sets

[42] The model versus observations agreement on the presence or absence of dust within a same profile is about 60 to 80% (Table 4), with higher values far from the sources. Nevertheless the main part of the sub–data set "agreement" is due to clear profiles (absence of dust). Consequently, this agreement is slightly higher in winter when there is less mineral dust than in summer. The sub–data set where both model and observation agree on the presence of dust somewhere within the same atmospheric column at the same time represents typically 35–47% of the profiles above emission regions and 7% above nonemissions (Table 4). It means that they are emitted at the good time and location half of the time; the first part of the transport is correct (inland) but their transport over seas is

Table 3. Mean Characteristics of the Nighttime Observed and Modeled Dust Layers[a]

	LBR_{int} (km)	LBR_{max} (ad.)	z_m (km)	*th* (km)	z_l (km)	z_t (km)
Observations Mean Values						
EMI W	2.2	2.3	1.8	1.2	1.1	2.5
EMI S	4.2	2.3	3.2	2.3	1.6	4.3
noEMI W	1.6	2.6	2.5	0.7	2.0	2.9
noEMI S	2.3	2.5	2.7	1.1	1.9	3.3
Model Mean Values						
EMI W	4.0	1.8	2.2	2.6	1.0	3.7
EMI S	5.1	1.7	4.8	3.2	3.0	6.3
noEMI W	3.2	1.6	3.3	2.2	2.1	4.5
noEMI S	3.6	1.5	3.7	2.6	2.3	5.0

[a]Values are presented separately for the emission regions (EMI) and the regions outside the emissions domain (noEMI) during winter (W) and summer (S). The scores are for LBR_{int} (kilometers), LBR_{max} (adimensional), and z_m, *th*, z_t, and z_l (kilometers).

21562202d, 2009, D9, Downloaded from https://agupubs.onlinelibrary.wiley.com/doi/10.1029/2008JD011219 by Cochrane France, Wiley Online Library on [02/06/2023]. See the Terms and Conditions (https://onlinelibrary.wiley.com/terms-and-conditions) on Wiley Online Library for rules of use; OA articles are governed by the applicable Creative Commons License

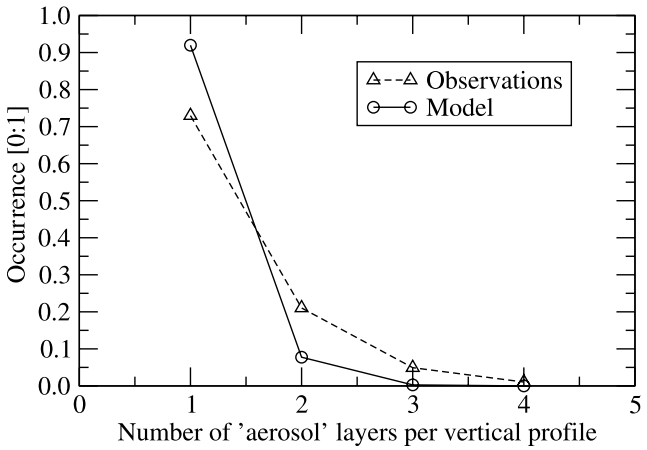

Figure 7. Distribution of number of separate dust layers in dust profiles for model and observations. Calculations are done for the summer nighttime data set.

not well reproduced by the model. The modeled and observed dust vertical structure for the sub–data set of profiles where model and observations agree on the presence of dust is studied here after.

7.2. Dust Vertical Distribution for the Collocated Data Sets

7.2.1. Mean Values

[43] The differences between model and dust vertical structures are reported in Figure 9 as histograms and in Table 5 as synthesized scores. Figure 9 shows a relatively good agreement between model and observations despite some large spreads around the mean zero value, and some differences between EMI and noEMI regions. The largest model-observations differences are denoted for the LBR_{max}. The model exhibits lower values than shown in the observations, with a more pronounced tendency over noEMI area. This is quantified by a histogram peak value of LBR_{max}(model) − LBR_{max}(obs) = −1 in Figure 9 and a relative difference of −24/−27% over EMI and −37/−38% over noEMI areas. These latter percentages are very similar

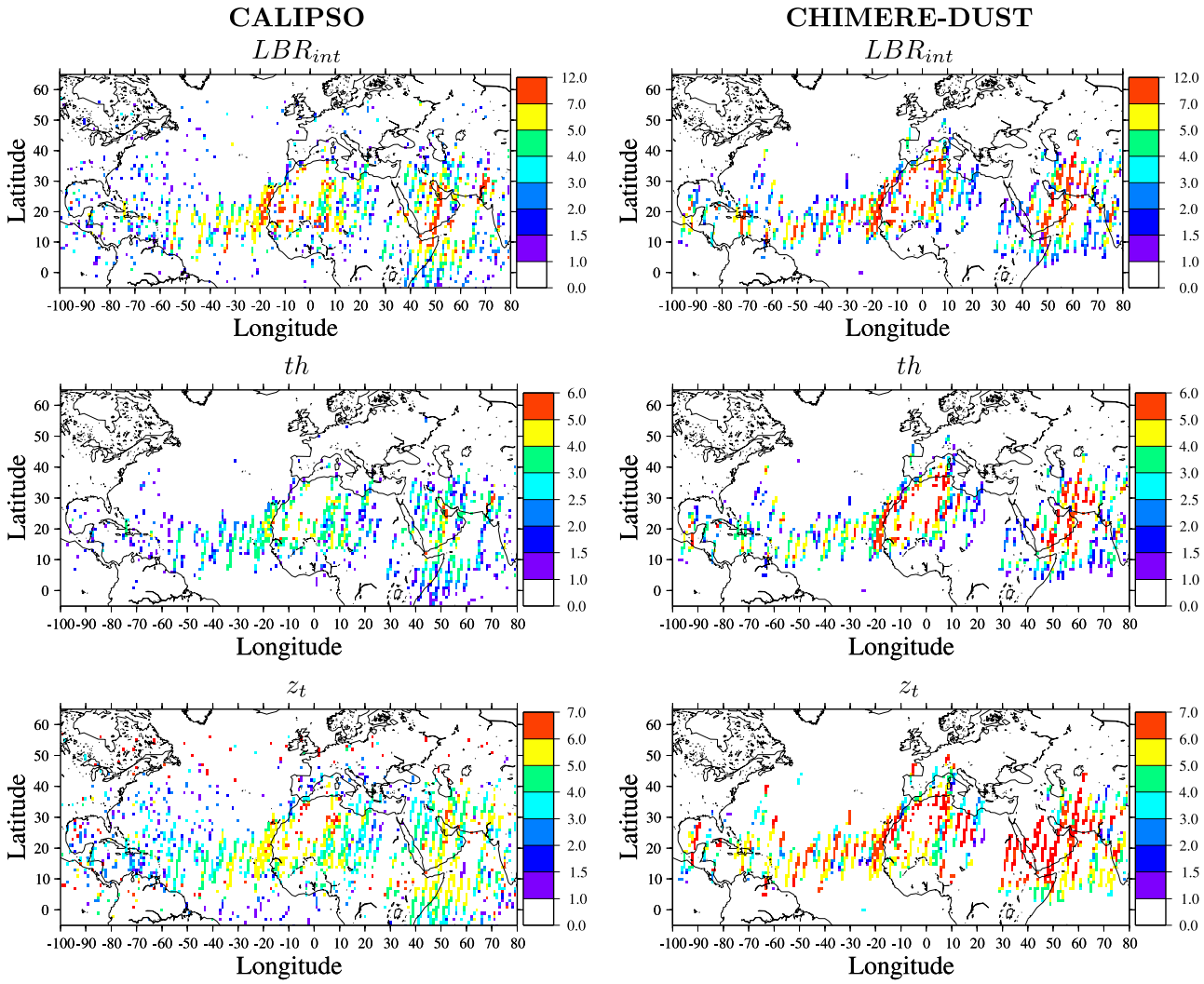

Figure 8. Maps of (top) LBR_{int}, (middle) "*th*" dust layer thickness (kilometers) and (bottom) z_t (kilometers) for the period 1 to 15 July 2006. Only nighttime data are used, and comparisons are presented for (left) the CALIPSO data and (right) the CHIMERE-DUST outputs.

21562202d, 2009, D9, Downloaded from https://agupubs.onlinelibrary.wiley.com/doi/10.1029/2008JD011219 by Cochrane France, Wiley Online Library on [02/06/2023]. See the Terms and Conditions (https://onlinelibrary.wiley.com/terms-and-conditions) on Wiley Online Library for rules of use; OA articles are governed by the applicable Creative Commons License

Table 4. Profiles Classification for Model and Observations[a]

		Agreement Model/Observations			Disagreement Model/Observations		
	Number of Profiles	Total	Mineral Dust	Clear	Total	Observations Dust Model Clear	Observations Clear Model Dust
			Winter				
EMI night	7506	66%	35%	31%	34%	22%	12%
EMI day	7696	56%	35%	21%	44%	29%	15%
noEMI night	35070	78%	6%	72%	22%	16%	6%
noEMI day	34769	65%	8%	57%	35%	30%	5%
			Summer				
EMI night	6896	62%	40%	22%	38%	22%	16%
EMI day	7553	63%	47%	16%	37%	23%	47%
noEMI night	36115	74%	7%	67%	26%	22%	4%
noEMI day	38817	57%	8%	49%	43%	40%	3%

[a]From left to the right: number of considered profiles (without high clouds or undefined values on the top) and percentage of profiles where model and observations agree on the presence/absence of dust, of profiles with both observed and modeled dust, of profiles where model and observations disagree on the presence/absence of dust, and of profiles with measured dust and not modeled ones.

to those obtained for the complete data set without collocation constraint (Table 3). The z_t and *th* overestimates by the model are of the same order of magnitude in the "collocated data set" and "noncollocated one." It indicates that the modeled vertical distribution is not very sensitive to the profile location. A large majority of the noEMI profiles are located over the Atlantic Ocean and in the free troposphere, where the atmosphere is strongly stratified. The

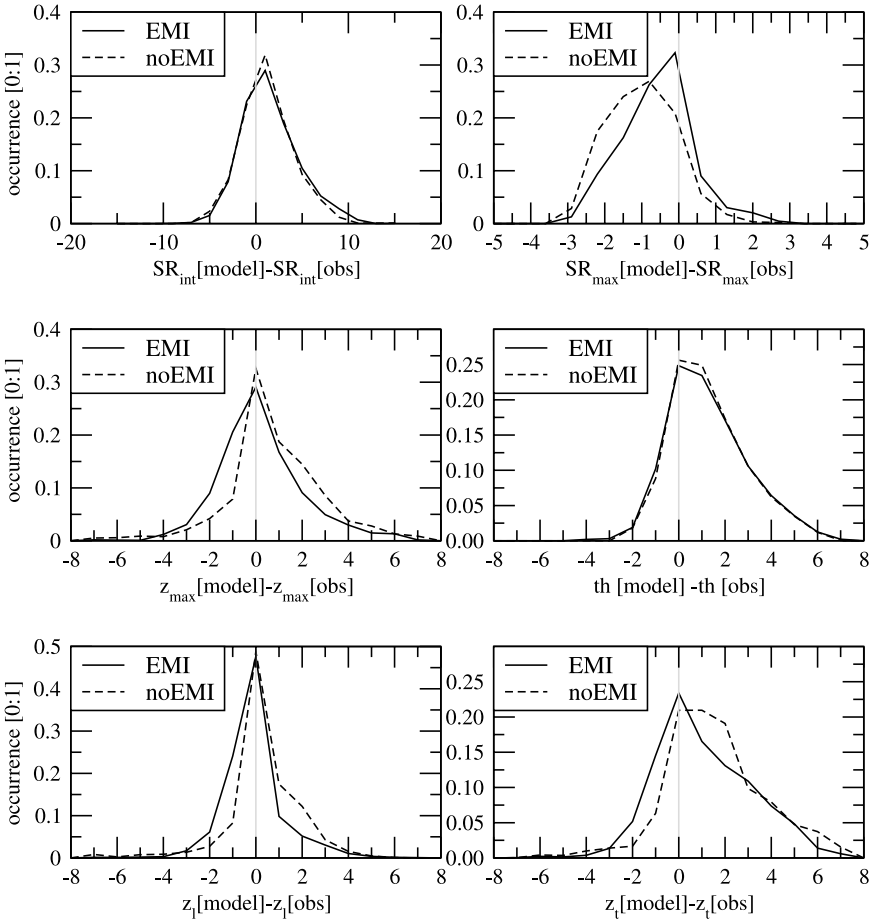

Figure 9. Histograms of model minus observations differences for the nights of the period from January to March 2007. Values are plotted for emissions regions (solid lines) and outside the emission regions (dashed lines). Results are presented as ΔLBR_{int}, ΔLBR_{max}, Δz_m (kilometers), Δth (kilometers), Δz_t (kilometers), and Δz_l (kilometers).

21562202d, 2009, D9, Downloaded from https://agupubs.onlinelibrary.wiley.com/doi/10.1029/2008JD011219 by Cochrane France, Wiley Online Library on [02/06/2023]. See the Terms and Conditions (https://onlinelibrary.wiley.com/terms-and-conditions) on Wiley Online Library for rules of use; OA articles are governed by the applicable Creative Commons License

Table 5. Model Versus Observations Mean Errors Estimated for the Periods January–March 2007 and June–September 2006 and for the Nighttime Data[a]

	$\frac{\Delta \text{int}}{\text{int}}$	$\frac{\Delta LBR_{\max}}{LBR_{\max}}$	$\frac{\Delta z_m}{z_m}$	$\frac{\Delta th}{th}$	$\frac{\Delta z_t}{z_t}$	$\frac{\Delta z_l}{z_l}$
EMI W	57%	−24%	12%	90%	41%	−10%
EMI S	21%	−27%	34%	40%	36%	47%
noEMI W	55%	−37%	37%	123%	57%	21%
noEMI S	14%	−38%	24%	52%	30%	22%

[a]The mean relative errors are displayed in percent and are split into EMI and noEMI regions.

vertical mesh used in the model is never able to reproduce the fine physics of thin dust layers long-range transport. Thus, owing to the nature of the algorithm used to described vertical transport, the concentrations fields are systematically more diffused in the model compared to the accurate measurements delivered by lidar measurements.

7.2.2. Diurnal Variation

[44] Summer (June–September 2006) mineral dust observations and simulations are compared to evaluate the diurnal variation of the vertical dynamics of the Saharan dust layer (Figure 10). Normalized occurrences for each LBR_{int} are displayed separately for the EMI and noEMI regions. Over the noEMI regions, the differences between day and night are lower than over EMI. This is due to the transport: far from the sources, the dust plumes are transported into the free troposphere and the diurnal cycle has no significant impact on the dust vertical structure. In this case, the LBR_{int} low values ≈1 are frequent (20–25%). Over the EMI area, the differences between night and day are much more pronounced: the maximum number of observed LBR values is for $LBR_{int} \approx 1$ during the day and $LBR_{int} \approx 6$ during the night. These differences show directly the impact of the wind speed diurnal cycle on dust emissions [*Menut*, 2008].

7.2.3. Seasonal Variation

[45] Figure 11 shows the LBR seasonal variability between winter and summer and highlights whether the model ability to reproduce observed events is strongly dependent on the season or not. For the two seasons, the dust amount distribution, LBR_{int}, is well estimated by the model. During summer, the model catches better this general evolution than during winter: with a very peaky value of $LBR_{int} \approx 1$ for the observations, the model shows a more spread-out distribution where a large part of wintertime modeled LBR_{int} are between 1 and 4. An opposite behavior is estimated for LBR_{max}: when the model calculated the largest part of LBR_{max} with values less than 2, observations are more equally distributed between 1 and 4. The same tendency is observed in winter and summer without significant impact of the season for LBR_{max}. The larger variability is denoted for the altitude of the LBR_{max} as already discussed with the Table 5: the differences between model and observations are large and depend on the period of the year. As a consequence of the dynamic processes occurring in the boundary layer (after the emissions and over land) and the free troposphere (mainly during dust long-range transport and over the ocean), the model has difficulties representing thin and highly concentrated dust layers at altitudes of less than 3 km. This certainly highlights the need to better represent vertical structure of thin layers in model as well as the transition between boundary layer and free troposphere when dust is trapped in more stratified layers at the end of each day.

8. Possible Sources of Errors

[46] The following defaults of the model were identified and quantified: (1) a tendency to overestimate plume

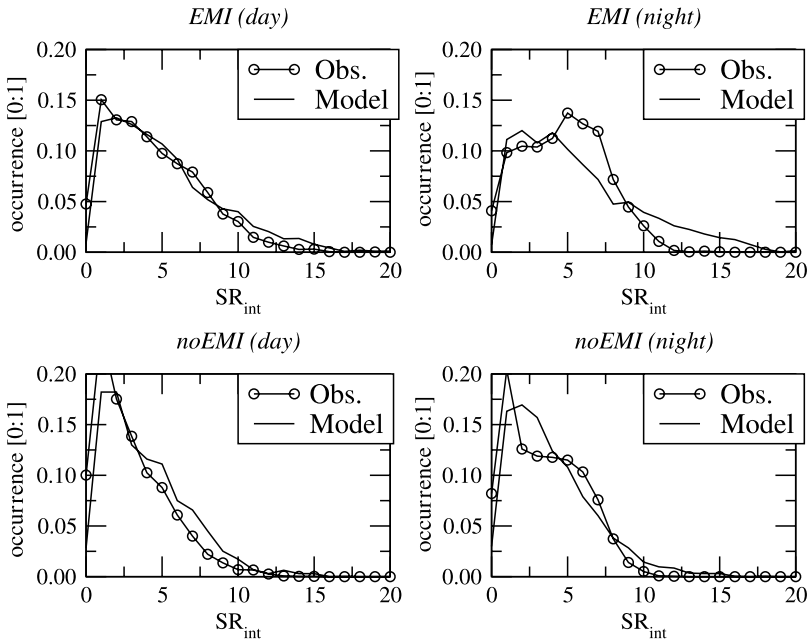

Figure 10. Diurnal variability of LBR_{int} over (top) the EMI area and (bottom) the noEMI area for the period June to September 2006.

21562202d, 2009, D9, Downloaded from https://agupubs.onlinelibrary.wiley.com/doi/10.1029/2008JD011219 by Cochrane France, Wiley Online Library on [02/06/2023]. See the Terms and Conditions (https://onlinelibrary.wiley.com/terms-and-conditions) on Wiley Online Library for rules of use; OA articles are governed by the applicable Creative Commons License

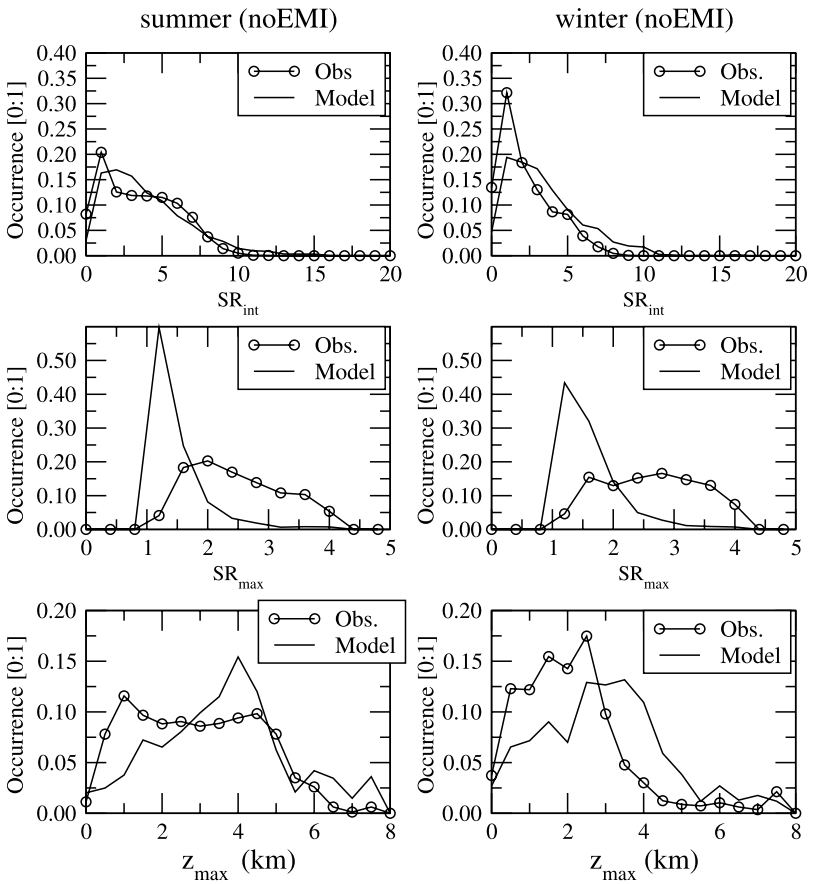

Figure 11. Analysis of the lidar backscattering ratio seasonal variability with nighttime data and model (over the noEMI region).

thickness and top height, (2) an underestimation of the LBR maximum value, (3) the difficulty to reproduce some complex multilayered structures. These limitations are first of all related to the model vertical resolution. Owing to computer limitations, the model is not able to run over a large domain and during a long period with a vertical resolution close to the real thin layers observed in the free troposphere. Thus, the modeled dust layers are vertically averaged layers and more able to be diffused vertically. Since the differences between th_{obs} and th_{mod} may be larger than the model resolution, the discrepancies may also be attributed to the vertical diffusion parameterization. As for many transport models used for air quality or long-range transport and climate, improvement on the vertical subgrid turbulence parameterizations is one of the most important challenges for the next years. The results presented in this paper show that the model simulates too strong vertical mixing, raising the simulated dust higher than the observed ones, missing multilayered structures, and smoothing the peaks of LBR. It has already been pointed out [*Noh et al.*, 2003] that one of the major shortcomings of the *Troen and Mahrt* [1986] parameterization of mixing is the fact that the eddy diffusivity depends only on surface stability and remains constant along the atmospheric column. Therefore a crucial phenomenon that could be taken into account is the vertical stabilization effect of the warmed dust layers, with the subsequent reduction of mixing. It is known indeed that the temperature of the Saharan dust layer is warmer than the normal tropical temperature by 5°–10°C [*Carlson and Prospero*, 1972]. This latter effect is not taken into account by any model.

[47] The horizontal pattern of the dust plumes can be considered instead quite well reproduced by the model. Besides, this pattern is mainly driven by the modeled horizontal wind fields, previously validated by many other studies [e.g., *White et al.*, 1999; *Hanna and Yang*, 2001; *Menut*, 2008]. Errors may also be due to the transport scheme itself: a recent study [*Vuolo et al.*, 2009] showed that this can be at the origin of some more or less diffused modeled horizontal dust plumes.

9. Conclusion

[48] Six months of CALIOP lidar data and CHIMERE-DUST modeled mineral dust concentrations fields are analyzed and compared. In order to have a homogeneous data set, lidar signal and dust concentrations values are processed to get the Lidar Scattering Ratio (LBR). For the observations and the model, data are over the same horizontal and vertical grid as the model, at the time of the satellite overpass along its trajectory.

[49] Criteria on LBR values are defined to discriminate the lidar profiles containing dust or clouds (or none or both) as a function of the time (night or day), the location (over

21562202d, 2009, D9, Downloaded from https://agupubs.onlinelibrary.wiley.com/doi/10.1029/2008JD011219 by Cochrane France, Wiley Online Library on [02/06/2023]. See the Terms and Conditions (https://onlinelibrary.wiley.com/terms-and-conditions) on Wiley Online Library for rules of use; OA articles are governed by the applicable Creative Commons License

the western Africa, near sources or over the Atlantic Ocean, far from the mineral dust sources), and the season (winter and summer). It was first shown that about 60% and 30% of the 170,000 observed profiles contained mineral dust (sometimes mixed with clouds), over the emissions and nonemissions regions, respectively. For the same data set, the model diagnosed 60% and 15% over the same regions. The difference between the two scores may be due to model data which cannot be contaminated by clouds, contrary to the observations.

[50] The vertical distribution and nature of the mineral dust layers was analyzed and compared: the thickest layers are observed during summer and over the emissions areas. The same tendency is calculated with the model even if this latter estimates highest absolute values. But the time and locations of the major events are well modeled compared to the measurements.

[51] The seasonal variability is weak compared to the sensitivity to the dust plume location. This is correctly reproduced by the model, clearly showing that the diurnal cycle is also moderated compared to the variability due to the range from the source.

[52] The seasonal variation of the dust as deduced by the observations is in agreement with previous studies: there is a summer northward shift of the regions of maximum dust occurrence (such as the one described by *D. Liu et al.* [2008]), and a summer increase of dust load (as in work by *Husar et al.* [1997] and *Kaufman et al.* [2005]) and the height reached by the dust (as in work by *Kishcha et al.* [2005], *Papayannis et al.* [2008], and *D. Liu et al.* [2008]). The model catches these behaviors even if the summer/winter ratio of integrated LBR (proportional to the dust load) is smaller in the model than in the observations (1.3 against 1.9 above the emission regions, 1.1 against 1.3 away from emission regions).

[53] The model is generally in better agreement with the observations in winter than summer. But the model always underestimates the maximum value of LBR within the profile and in average overestimates the vertical extension of the mineral dust in the column; this means that in the model most of the atmospheric layers contain a small amount of dust, whereas in the observations a few layers at a given altitude contain a large amount of mineral dust particles. Hence the model is not able to reproduce vertically confined layers of aerosols, and mostly produces small amount of dust spread within a too large vertical extent.

[54] Errors on the thickness of the mineral dust layers are on the order of 100% in winter and 50% in summer, while the maximum value of the lidar signal on a vertical profile is typically underestimated by 30%. Also, multilayered dust structures are typically missed by the model. All these discrepancies suggest that the model's vertical mixing is excessive, probably in conditions where it should be suppressed by the presence of the dust layers (the model at present does not take into account the radiative effect of aerosols and their eventual suppression of convective mixing).

[55] Finally, the model behaves quite well far from the emission regions. There is no noticeable disagreement with the observations there, except those which have already been identified above the emission regions and are slightly more pronounced far from the sources after dust long-range transport.

Appendix A: Lidar Signal

[56] The power of light backscattered by air molecules and aerosol particles at a distance z from the lidar depends on their number concentration $n_{mol/part}$ (m^{-3}) and on their scattering and absorption cross sections $C_{sca,mol/part}$, $C_{ext,mol/part}$ (m^2). The attenuated lidar backscattering profile, ATB (m^{-1} sr^{-1}), is given by the lidar equation

$$\mathrm{ATB}(z) = \left[\beta_{\mathrm{mol}}(z) + \beta_{\mathrm{part}}(z)\right] \times \exp\left\{-2\int_0^z \left[\alpha_{\mathrm{ext,mol}}(z) + \alpha_{\mathrm{ext,part}}(z)\right]dz\right\}, \quad \text{(A1)}$$

where $\beta_{mol/part}$ (m^{-1} sr^{-1}) are molecules (particles) backscattering coefficients, expressed as

$$\beta_{\mathrm{mol/part}} = \frac{P_{\pi,\mathrm{mol/part}}}{\pi} n_{\mathrm{mol/part}} C_{\mathrm{sca,mol/part}}, \quad \text{(A2)}$$

where $P_{\pi,mol/part}$ (sr^{-1}) are the phase functions in backscattering.

[57] The attenuation extinction (scattering+absorption) coefficients $\alpha_{ext,mol/part}$ (m^{-1}) are given by

$$\alpha_{\mathrm{ext,mol/part}} = n_{\mathrm{mol/part}} C_{\mathrm{ext,mol/part}}, \quad \text{(A3)}$$

with

$$C_{\mathrm{ext,mol/part}} = C_{\mathrm{sca,mol/part}} + C_{\mathrm{abs,mol/part}}. \quad \text{(A4)}$$

[58] The absorption cross section $C_{abs,mol}$ is negligible for air molecules at 532 and 1064 nm.

[59] Following *Collis and Russell* [1976] scattering and attenuation coefficients for molecules β_{mol}, α_{mol} can be expressed as

$$\beta_{\mathrm{mol}} = \frac{P}{kT}\left(5.45 \cdot 10^{-32}\right)\left(\frac{\lambda}{0.55}\right)^{-4.09} \quad \text{(A5)}$$

$$\alpha_{\mathrm{mol}} = \frac{\beta_{mol}}{0.119}, \quad \text{(A6)}$$

where λ is the wavelength of the incident light, P and T are pressure and temperature, and k is the Boltzmann constant.

[60] To highlight the contribution of aerosols, the lidar signal is normalized to the molecular one, leading to the (adimensional) lidar backscattering ratio,

$$\mathrm{LBR} = \frac{\mathrm{ATB}}{\mathrm{ATB_{mol}}}. \quad \text{(A7)}$$

where

$$\mathrm{ATB_{mol}}(z) = \beta_{\mathrm{mol}}(z) \exp\left[-2\int_0^z \alpha_{\mathrm{ext,mol}}(z)dz\right]. \quad \text{(A8)}$$

[61] By definition, LBR $\equiv$ 1 in clear-sky conditions ($\beta_{part} = \alpha_{part} = 0$).

21562202d, 2009, D9, Downloaded from https://agupubs.onlinelibrary.wiley.com/doi/10.1029/2008JD011219 by Cochrane France, Wiley Online Library on [02/06/2023]. See the Terms and Conditions (https://onlinelibrary.wiley.com/terms-and-conditions) on Wiley Online Library for rules of use; OA articles are governed by the applicable Creative Commons License

[62] **Acknowledgments.** Thanks are owed to NASA, CNES, ICARE, and CLIMSERV (with Karim Ramage and Sophie Cloché) for giving access to the CALIOP level 1 data. Three anonymous reviewers are acknowledged for their useful comments.

References

Alfaro, S. C., and L. Gomes (2001), Modeling mineral aerosol production by wind erosion: Emission intensities and aerosol size distribution in source areas, *J. Geophys. Res.*, *106*(D16), 18,075–18,084.

Alpert, P., P. Kishcha, A. Shtivelman, S. O. Krichak, and J. H. Joseph (2004), Vertical distribution of Saharan dust based on 2.5-year model predictions, *Atmos. Res.*, *70*, 109–130.

Amiridis, V., et al. (2007), Aerosol lidar observations and model calculations of the planetary boundary layer evolution over Greece, during the March 2006 total solar eclipse, *Atmos. Chem. Phys.*, *7*, 6181–6189.

Ansmann, A., et al. (2003), Long-range transport of Saharan dust to northern Europe: The 11–16 October 2001 outbreak with EARLINET, *J. Geophys. Res.*, *108*(D24), 4783, doi:10.1029/2003JD003757.

Barnaba, F., A. M. Tafuro, F. De Tomasi, and M. R. Perrone (2007), Observed and simulated vertically resolved optical properties of continental aerosols over southestern Italy: A closure study, *J. Geophys. Res.*, *112*, D10203, doi:10.1029/2006JD007926.

Bessagnet, B., A. Hodzic, R. Vautard, M. Beekmann, S. Cheinet, C. Honoré, C. Liousse, and L. Rouil (2004), Aerosol modeling with CHIMERE: Preliminary evaluation at the continental scale, *Atmos. Environ.*, *38*, 2803–2817.

Bey, I., D. J. Jacob, R. M. Yantosca, J. A. Logan, B. D. Field, A. M. Fiore, Q. Li, H. Y. Liu, L. J. Mickley, and M. G. Schultz (2001), Global modeling of tropospheric chemistry with assimilated meteorology: Model description and evaluation, *J. Geophys. Res.*, *106*(D19), 23,073–23,096.

Bouet, C., G. Cautenet, R. Washington, M. Todd, B. Laurent, B. Marticorena, and G. Bergametti (2007), Mesoscale modeling of Aeolian dust emission during the BoDEx 2005 experiment, *Geophys. Res. Lett.*, *34*, L07812, doi:10.1029/2006GL029184.

Carlson, T., and J. Prospero (1972), The large-scale movement of Saharan air outbreaks over the northern equatorial Atlantic, *J. Appl. Meteorol.*, *11*, 283–297.

Chepfer, H., M. Chiriaco, R. Vautard, and J. Spinhirne (2007), Evaluation of the ability of MM5 meso-scale model to reproduce optically thin clouds over Europe in fall using ICE/SAT lidar space-born observations, *Mon. Weather Rev.*, *135*, 2737–2753.

Chepfer, H., S. Bony, D. Winker, M. Chiriaco, J.-L. Dufresne, and G. Sèze (2008), Use of CALIPSO lidar observations to evaluate the cloudiness simulated by a climate model, *Geophys. Res. Lett.*, *35*, L15704, doi:10.1029/2008GL034207.

Chiriaco, M., R. Vautard, H. Chepfer, M. Haeffelin, Y. Wanherdrick, Y. Morille, A. Protat, J. Dudhia, and C. F. Mass (2006), The ability of MM5 to simulate thin ice clouds: Systematic comparisons with lidar/radar and fluxes measurements, *Mon. Weather Rev.*, *134*, 897–918.

Colette, A., G. Ancellet, L. Menut, and S. R. Arnold (2006), A Lagrangian analysis of the impact of transport and transformation on the ozone stratification observed in the free troposphere during the ESCOMPTE campaign, *Atmos. Chem. Phys.*, *6*, 3487–3503.

Collis, R. T. H., and P. B. Russell (1976), Lidar measurement of particles and gases by elastic backscattering and differential absorption, *Topics Appl. Phys.*, *14*, 71–151.

d'Almeida, G. A. (1986), A model for Saharan dust transport, *J. Appl. Meteorol.*, *25*, 903–916.

Dayan, U., B. Ziv, T. Shoob, and Y. Enzel (2008), Suspended dust over southeastern Mediterranean and its relation to atmospheric circulations, *Int. J. Climatol.*, *28*, 915–924, doi:10.1002/joc.1587.

Duce, R. (1995), Sources, distributions, and fluxes of mineral aerosols and their relationship to climate, in *Aerosol Forcing of Climate*, edited by R. J. Charlson and J. Heintzenberg, pp. 43–72, John Wiley, Chichester, U. K.

Dudhia, J. (1993), A nonhydrostatic version of the Penn State/NCAR mesoscale model: Validation tests and simulation of an Atlantic cyclone and cold front, *Mon. Weather Rev.*, *121*, 1493–1513.

Forêt, G., G. Bergametti, F. Dulac, and L. Menut (2006), An optimized particle size bin scheme for modeling mineral dust aerosol, *J. Geophys. Res.*, *111*, D17310, doi:10.1029/2005JD006797.

Ginoux, P., J. M. Prospero, O. Torres, and M. Chin (2004), Long-term simulation of global dust distribution with the GOCART model: Correlation with North Atlantic Oscillation, *Environ. Modell. Software*, *19*, 113–128.

Grini, A., P. Tulet, and L. Gomes (2006), Dusty weather forecasts using the MesoNH mesoscale atmospheric model, *J. Geophys. Res.*, *111*, D19205, doi:10.1029/2005JD007007.

Guelle, W., Y. J. Balkanski, B. Shulz, M. Marticorena, G. Bergametti, C. Moulin, R. Arimoto, and K. D. Perry (2000), Modeling the atmospheric distribution of mineral aerosol: Comparison with ground measurements and satellite observations for yearly and synoptic timescales over the North Atlantic, *J. Geophys. Res.*, *105*(D2), 1997–2012.

Hamonou, E., P. Chazette, D. Balis, F. Dulac, X. Schneider, E. Galani, G. Ancellet, and A. Papayannis (1999), Characterization of the vertical structure of Saharan dust export to the Mediterranean basin, *J. Geophys. Res.*, *104*(D18), 22,257–22,270, doi:10.1029/1999JD900257.

Hanna, S. R., and R. Yang (2001), Evaluations of mesoscale models' simulations of near-surface winds, temperature gradients, and mixing depths, *J. Appl. Meteorol.*, *40*, 1095–1104.

Hara, Y., K. Yumimoto, I. Uno, A. Shimizu, N. Sugimoto, Z. Liu, and D. M. Winker (2008), Asian dust outflow in the PBL and free atmosphere retrieved by NASA CALIPSO and an assimilated dust transport model, *Atmos. Chem. Phys. Discuss.*, *8*, 8715–8742.

Heinold, B., J. Helmert, O. Hellmuth, R. Wolke, A. Ansmann, B. Marticorena, B. Laurent, and I. Tegen (2007), Regional modeling of Saharan dust events using LM-MUSCAT: Model description and case studies, *J. Geophys. Res.*, *112*, D11204, doi:10.1029/2006JD007443.

Hodzic, A., et al. (2004), Comparisons of aerosol chemistry-transport model simulations with lidar and Sun photometer observations at a site near Paris, *J. Geophys. Res.*, *109*, D23201, doi:10.1029/2004JD004735.

Husar, R. B., J. M. Prospero, and L. L. Stowe (1997), Characterization of tropospheric aerosols over the oceans with the NOAA advanced very high resolution radiometer optical thickness operational product, *J. Geophys. Res.*, *102*(D14), 16,889–16,910, doi:10.1029/96JD04009.

Kalashnikova, O. V., and R. A. Kahn (2008), Mineral dust plume evolution over the Atlantic from MISR and MODIS aerosol retrievals, *J. Geophys. Res.*, *113*, D24204, doi:10.1029/2008JD010083.

Karyampudi, V., et al. (1999), Validation of the Saharan dust plume conceptual model using lidar, Meteosat, and ECMWF data, *Bull. Am. Meteorol. Soc.*, *80*, 1045–1075.

Kaufman, Y. J., I. Koren, L. A. Remer, D. Tanré, P. Ginoux, and S. Fan (2005), Dust transport and deposition observed from the Terra-Moderate Resolution Imaging Spectroradiometer (MODIS) spacecraft over the Atlantic Ocean, *J. Geophys. Res.*, *110*, D10S12, doi:10.1029/2003JD004436.

Kim, S.-W., S. Berthier, J.-C. Raut, P. Chazette, F. Dulac, and S.-C. Yoon (2008), Validation of aerosol and cloud layer structures from the space-borne lidar CALIOP using a ground-based lidar in Seoul, Korea, *Atmos. Chem. Phys.*, *8*, 3705–3720.

Kishcha, P., F. Barnaba, G. P. Gobbi, P. Alpert, A. Shtivelman, S. O. Krichak, and J. H. Joseph (2005), Vertical distribution of Saharan dust over Rome (Italy): Comparison between 3-year model predictions and lidar soundings, *J. Geophys. Res.*, *110*, D06208, doi:10.1029/2004JD005480.

Liu, D., Z. Wang, Z. Liu, D. Winker, and C. Trepte (2008), A height resolved global view of dust aerosols from the first year CALIPSO lidar measurements, *J. Geophys. Res.*, *113*, D16214, doi:10.1029/2007JD009776.

Liu, Z., et al. (2008a), CALIPSO lidar observations of the optical properties of Saharan dust: A case study of long-range transport, *J. Geophys. Res.*, *113*, D07207, doi:10.1029/2007JD008878.

Liu, Z., et al. (2008b), Airborne dust distributions over the Tibetan Plateau and surrounding areas derived from the first year of CALIPSO lidar observations, *Atmos. Chem. Phys.*, *8*, 5045–5060.

Loosmore, G., and R. Cederwall (2004), Precipitation scavenging of atmospheric aerosols for emergency response applications: Testing an updated model with new real-time data, *Atmos. Environ.*, *38*, 993–1003.

Marticorena, B., and G. Bergametti (1995), Modeling the atmospheric dust cycle: 1. Design of a soil-derived dust production scheme, *J. Geophys. Res.*, *100*(D8), 16,415–16,430.

Menut, L. (2003), Adjoint modeling for atmospheric pollution processes sensitivity at regional scale, *J. Geophys. Res.*, *108*(D17), 8562, doi:10.1029/2002JD002549.

Menut, L. (2008), Sensitivity of hourly saharan dust emissions to NCEP and ECMWF modeled wind speed, *J. Geophys. Res.*, *113*, D16201, doi:10.1029/2007JD009522.

Menut, L., C. Schmechtig, and B. Marticorena (2005), Sensitivity of the sandblasting fluxes calculations to the soil size distribution accuracy, *J. Atmos. Oceanic Technol.*, *22*, 1875–1884.

Menut, L., G. Foret, and G. Bergametti (2007), Sensitivity of mineral dust concentrations to the model size distribution accuracy, *J. Geophys. Res.*, *112*, D10210, doi:10.1029/2006JD007766.

Mie, G. (1908), Beitrage zur Optik traber Medien, speziell kolloidaler Metallasungen, *Ann. Phys.*, *330*, 377–445.

Mikami, M., et al. (2006), Aeolian dust experiment on climate impact: An overview of Japan China joint project ADEC, *Global Planet. Change*, *52*, 142–172, doi:10.1016/j.gloplacha.2006.03.001.

Mona, L., A. Amodeo, M. Pandolfi, and G. Pappalardo (2006), Saharan dust intrusions in the Mediterranean area: Three years of lidar measurements in Potenza, *J. Geophys. Res.*, *111*, D16203, doi:10.1029/2005JD006569.

21562202d, 2009, D9, Downloaded from https://agupubs.onlinelibrary.wiley.com/doi/10.1029/2008JD011219 by Cochrane France, Wiley Online Library on [02/06/2023]. See the Terms and Conditions (https://onlinelibrary.wiley.com/terms-and-conditions) on Wiley Online Library for rules of use; OA articles are governed by the applicable Creative Commons License

Noh, Y., W. G. Cheon, S. Y. Hong, and S. Raasch (2003), Improvement of the K-profile Model for the planetary boundary layer based on large eddy simulation data, *Boundary Layer Meteorol.*, *107*, 401–427.

Papayannis, A., et al. (2008), Systematic lidar observations of Saharan dust over Europe in the frame of EARLINET (2000–2002), *J. Geophys. Res.*, *113*, D10204, doi:10.1029/2007JD009028.

Prospero, J. M., R. A. Glaccum, and R. T. Nees (1981), Atmospheric transport of soil dust from Africa to South America, *Nature*, *289*, 570–572, doi:10.1038/289570a0.

Prospero, J. M., K. Barrett, T. Church, F. Dentener, R. A. Duce, J. N. Galloway, H. Levy, J. Moody, and P. Quinn (1996), Atmospheric deposition of nutrients to the North Atlantic Basin, *Biogeochemistry*, *35*, 27–73.

Prospero, J. M., P. Ginoux, O. Torres, S. E. Nicholson, and T. E. Gill (2002), Environmental characterization of global sources of atmospheric soil dust identified with the NIMBUS 7 total ozone mapping spectrometer (TOMS) absorbing aerosol products, *Rev. Geophys.*, *40*(1), 1002, doi:10.1029/2000RG000095.

Shinn, E. A., G. W. Smith, J. M. Prospero, P. Betzer, M. L. Hayes, V. Garrison, and R. T. Barber (2000), African dust and the demise of caribbean coral reefs, *Geophys. Res. Lett.*, *27*, 3029–3032, doi:10.1029/2000GL011599.

Sokolik, I., D. M. Winker, G. Bergametti, D. A. Gillette, G. Carmichael, Y. Kaufman, L. Gomes, L. Schuetz, and J. E. Penner (2001), Outstanding problems in quantifying the radiative impact of mineral dust, *J. Geophys. Res.*, *106*(D16), 18,015–18,028.

Troen, I., and L. Mahrt (1986), A simple model of the atmospheric boundary layer: Sensitivity to surface evaporation, *Boundary Layer Meteorol.*, *37*, 129–148.

Uno, I., K. Yumimoto, A. Shimizu, N. Hara, Y. Sugimoto, Z. Wang, Z. Liu, and D. M. Winker (2008), 3D structure of Asian dust transport revealed by CALIPSO lidar and a 4DVAR dust model, *Geophys. Res. Lett.*, *35*, L06803, doi:10.1029/2007GL032329.

Van Leer, B. (1979), Towards the ultimate conservative difference scheme. V A second order sequel to Godunov's method, *J. Comput. Phys.*, *32*, 101–136.

Vautard, R., M. Beekmann, J. Roux, and D. Gombert (2001), Validation of a hybrid forecasting system for the ozone concentrations over the Paris area, *Atmos. Environ.*, *35*, 2449–2461.

Venkatram, A., and J. Pleim (1999), The electrical analogy does not apply to modeling dry deposition of particles, *Atmos. Environ.*, *33*, 3075–3076.

Vuolo, M., L. Menut, and H. Chepfer (2009), Impact of transport schemes on modelled dust concentrations, *J. Atmos. Oceanic Technol.*, doi:10.1175/2008JTECHA1197.1, in press.

White, B. G., J. Paegle, W. J. Steenburgh, J. D. Horel, R. T. Swanson, L. K. Cook, D. J. Onton, and J. G. Miles (1999), Short-term forecast validation of six models, *Weather Forecast.*, *14*, 84–108.

Winker, D. M., W. H. Hunt, and M. J. McGill (2007), Initial performance assessment of CALIOP, *Geophys. Res. Lett.*, *34*, L19803, doi:10.1029/2007GL030135.

Zhu, A., V. Ramanathan, F. Li, and D. Kim (2007), Dust plumes over the Pacific, Indian, and Atlantic oceans: Climatology and radiative impact, *J. Geophys. Res.*, *112*, D16208, doi:10.1029/2007JD008427.

G. Cesana and L. Menut, Laboratoire de Météorologie Dynamique, Ecole Polytechnique, CNRS F-91128 Palaiseau, France.

H. Chepfer, Laboratoire de Météorologie Dynamique, Université Pierre et Marie Curie, 4 Place Jussieu, F-75252 Paris, France.

M. R. Vuolo, Laboratoire de Météorologie Dynamique, Ecole Polytechnique, F-91128 Palaiseau, France. (vuolo@lmd.polytechnique.fr)

21562202d, 2009, D9, Downloaded from https://agupubs.onlinelibrary.wiley.com/doi/10.1029/2008JD011219 by Cochrane France, Wiley Online Library on [02/06/2023]. See the Terms and Conditions (https://onlinelibrary.wiley.com/terms-and-conditions) on Wiley Online Library for rules of use; OA articles are governed by the applicable Creative Commons License